Hindawi
Advances in Mathematical Physics
Volume 2023, Article ID 2088607, 16 pages
https://doi.org/10.1155/2023/2088607

Research Article

Free Convection Heat Transfer in Composite Enclosures with Porous and Nanofluid Layers

Abeer Alhashash

Science Department, Jouf University, Sakaka Aljawf 24241, Saudi Arabia

Correspondence should be addressed to Abeer Alhashash; ahashash@ju.edu.sa

Received 28 September 2023; Revised 18 November 2023; Accepted 27 November 2023; Published 11 December 2023

Academic Editor: Mahnoor Sarfraz

This work conducts a numerical investigation of convection heat transfer within two composite enclosures. These enclosures consist of porous and nanofluidic layers, where the porous layers are saturated with the same nanofluid. The first enclosure has two porous layers of different sizes and permeabilities, while the second is separated by a single porous layer. As the porous layer thickness approaches zero, both enclosures transition to clear nanofluid enclosures. The study uses the Navier–Stokes equations to govern fluid flow in the nanofluid domain and the Brinkman–Forchheimer extended Darcy model to describe flow within the saturated porous layer. Numerical solutions are obtained using an iterative finite difference method. Key parameters studied include the porous thickness ($0.0 \le S \le 1.0$), the nanoparticle volume fraction ($0.0 \le \phi \le 0.05$), the thermal conductivity ratio ($0.5 \le R_k \le 10$), and the Darcy number ($10^{-5} \le Da \le 10^{-2}$). Key findings include the observation that the highest heat transfer is achieved at the highest concentration, regardless of the porous layer configuration, permeability value, or thermal conductivity ratio. Specifically, an augmentation in values of $\overline{Nu}_{\mathrm{I}}$ up to 22% is obtained as concentration is adjusted from 1% to 5%. Similarly, an augmentation in values of $\overline{Nu}_{\mathrm{II}}$ up to 25% is obtained as concentration is adjusted from 1% to 5%.

1. Introduction

Convection heat transfer is a process in which heat is transferred by the movement of the working fluids. The working fluid can be water, gas, or nanofluids. Nanofluids are colloidal suspensions of nanoparticles in a base fluid. The nanoparticles can be made of a variety of materials, such as metals, oxides, or semiconductors. Nanofluids have been shown by Choi [1] to have enhanced thermal conductivity compared to the base fluid. Bourantas et al. [2] concluded that the role of nanofluids has promising future applications in cooling technology. Mahdi et al. [3] summarized that as the volume concentration of nanoparticles increased, published studies reported a prominent improvement in heat transfer. Duwairi et al. [4] showed that the use of nanofluids combined with porous media improves the performance of the evacuated tube when compared to the use of water alone. The nanofluid can be applied to the composite enclosures. Composite enclosures are porous materials that contain a high volume of voids or pores. These pores can be filled with air, water, or other fluids. Porous materials can have a significant impact on heat transfer, as they can provide additional pathways for fluid flow and heat conduction [5–8].

Convection heat transfer in composite enclosures has gained significant attention due to its relevance in various engineering applications. The combination of porous and nanofluid layers in these enclosures offers unique thermal characteristics and presents an opportunity for enhanced heat transfer performance. The focus of this study is to investigate the convection heat transfer behavior in two composite enclosures where the porous layers are saturated with the same nanofluid. The choice of using porous layers is motivated by their ability to control and manipulate fluid flow, while nanofluids, which are colloidal suspensions of nanoparticles in a base fluid, exhibit promising thermal properties. Efficient thermal management is essential for maintaining comfortable indoor environments and reducing energy consumption in buildings and HVAC (heating, ventilation, and air conditioning) systems. Composite enclosures with porous and nanofluid layers can be utilized in insulation materials, walls, and windows to enhance heat transfer control. The findings from this study can guide the development of

improved building materials and HVAC systems, leading to energy savings and increased occupant comfort. The composite enclosures with porous and nanofluid layers are also relevant in solar energy applications. By optimizing the convective heat transfer process within these enclosures, the efficiency of solar collectors and heat exchangers can be improved. This can lead to enhanced energy conversion and utilization, making solar energy systems more viable and sustainable.

Many studies have been published on the theoretical and experimental study of nanofluid flow and heat transfer in composite enclosures. Chamkha and Ismael [9] have arranged the porous layer and nanofluid layer side by side. Later, Ismael and Chamkha [10], Tahmasebi et al. [11], and Mehryan et al. [12] attached a solid wall to the porous layer side. Alsabery et al. [13, 14] found the increase in the porous layer has a significant impact on heat transport. Toosi and Siavashi [15] concluded that at heating intensity, it is not suggested to use a nanofluid with a porous medium. Al-Zamily [16] concluded that as the thickness of the porous media layer decreases, so does the maximum streamfunction. The interaction of the corrugated surface with the combination of permeabilities and nanoparticles has been studied by Nguyen et al. [17], Alsabery et al. [18], and Kadhim et al. [19]. Miroshnichenko et al. [20] studied the effect of porous layers on natural convection in an open enclosure and found the thermal augmentation with nanoparticle concentration for low left nanofluid layer thickness values. Al-Srayyih et al. [21] and Chamkha et al. [22] filled the composite enclosure with a hybrid nanofluid and applied a local thermal nonequilibrium model for the heat transfer between the nanofluid and the solid phases. Raizah et al. [23] focused on the convective flow inside nonrectangular enclosures. Recently, Selimefendigil and Chamkha [24] found significant changes in the average Nusselt number, which are obtained by varying the location of the porous medium. Ghalambaz et al. [25] and Ghalambaz et al. [26] investigated the thermal performance of nanoencapsulated phase change material suspension in the composite enclosure. Recently, Aly and Alsedais [27] concluded that at lower Darcy parameters, the existence of a porous sheet in the right region inhibits the suspension flow in this region.

In summary, prior research has highlighted the potential of composite enclosures with porous and nanofluid layers for enhanced convective heat transfer. The studies discussed in the above literature review have focused on different aspects of these composite enclosures, including the effects of porous structures and their location and nanofluid characteristics. However, no information has been obtained for a systematic comparison of composite enclosures that have two porous layers, and one is separated by a porous layer. The present study aims to contribute to this body of knowledge by numerically investigating the convection heat transfer behavior in two composite enclosures. The first kind of composite enclosure has two porous layers with varying sizes and permeabilities. This configuration allows us to explore the influence of different porous structures on the convective heat transfer process. The second composite enclosure, on the other hand, is partitioned by a porous layer, providing an additional element to investigate the impact of porous barriers on fluid flow and heat transfer. The first and second composite enclosures can be employed in architectural and HVAC system planning. These porous materials are effective in purifying fluids from impurities, mitigating noise, maintaining temperature, and lessening the necessity for mechanical heating and cooling. In HVAC systems, porous substances can serve as heat exchangers or evaporative coolers. Configuration options I or II can be customized to fit particular requirements. To optimize material efficiency, it is important to ensure that the combined heat and mass volume of the porous material remains consistent, irrespective of the construction design. Investigating the heat transfer characteristics in such complex configurations can provide valuable insights into the interactions between the porous layers, fluid flow patterns, and heat transfer rates, leading to a more comprehensive understanding of convective heat transfer in composite enclosures. The analysis in this study focuses on investigating the effects of various dimensionless parameters on convective heat transfer in both enclosures.

2. Mathematical Formulation

A schematic diagram of two composite enclosures with sides of length L is shown in Figure 1. Two porous layers with various sizes and permeabilities are attached to enclosure I. The enclosure II is partitioned or divided by a porous layer. Both porous layers have the same thickness at s. When the porous layer approaches zero, both enclosures evolve into clear-fluid enclosures, and while the porous thickness goes to s, both enclosures are fully filled with a saturated porous medium. The hot wall is set to the left. Opposite the hot wall is the cold wall. The other two walls are maintained at insulated condition. Both sides are filled with nanofluid, Al_2O_3, and water.

All interfaces between the fluid and porous layers are permeable, and the wall enclosures are impermeable. Thermophysical properties of the nanofluid in the flow field are assumed to be constant except for the density variations causing a body force term in the momentum equation. The Boussinesq approximation is invoked for the nanofluid properties to relate density changes to temperature changes, and to couple in this way the temperature field to the flow field. The Brinkman–Forchheimer equation is used to model the porous medium flow. Vertical fluid/porous layer interfaces are permeable. All external boundaries are impermeable. Influences of thermophoresis, radiation, viscous dissipation, and Joule heating are neglected. A solid, porous matrix and a saturating fluid are in a state of thermal equilibrium, as modeled by Elliott et al. [28]. Under these assumptions, the governing equations for steady natural convection flow using conservation of mass, momentum, and energy can be written as follows:

$$\frac{\partial u_f}{\partial x} + \frac{\partial v_f}{\partial y} = 0, \tag{1}$$

$$u_f \frac{\partial u_f}{\partial x} + v_f \frac{\partial u_f}{\partial y} = -\frac{1}{\rho_{nf}} \frac{\partial p_f}{\partial x} + \frac{\mu_{nf}}{\rho_{nf}} \left(\frac{\partial^2 u_f}{\partial x^2} + \frac{\partial^2 u_f}{\partial y^2} \right), \tag{2}$$

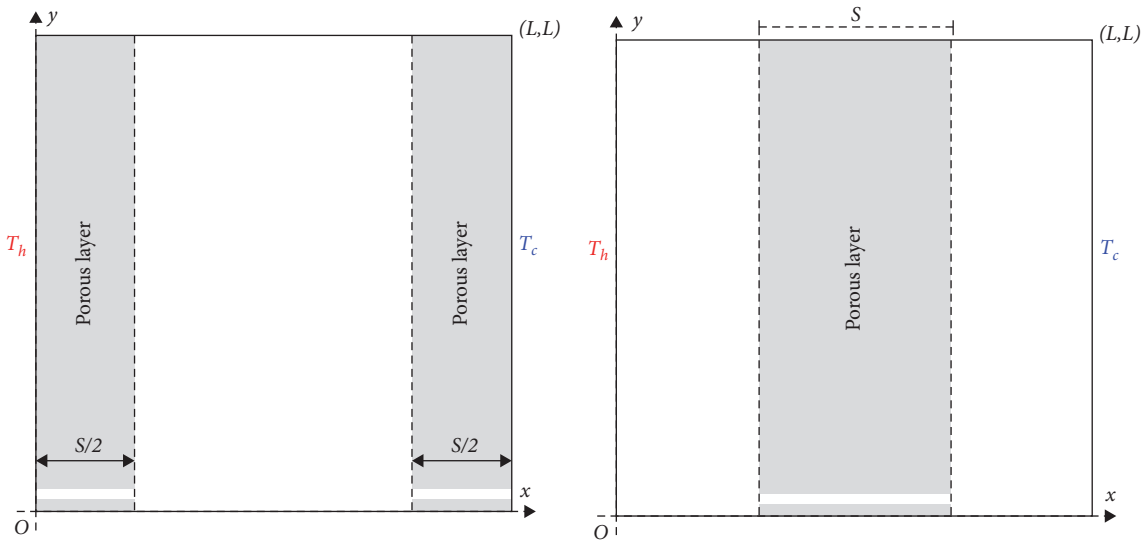

FIGURE 1: Schematic representation of the enclosure I (a) and enclosure II (b).

TABLE 1: Thermophysical properties of the nanofluids used in this work.

Materials	Water	Al_2O_3
Specific heat capacity, C_p ($J\,kg^{-1}\,K^{-1}$)	4,179	765
Density, ρ ($kg\,m^{-3}$)	997.1	3,970
Thermal conductivity, k ($W\,m^{-1}\,K^{-1}$)	0.613	40
Thermal expansion coefficient, β (K^{-1})	21×10^{-5}	0.85×10^{-5}

$$u_f\frac{\partial v_f}{\partial x}+v_f\frac{\partial v_f}{\partial y}=-\frac{1}{\rho_{nf}}\frac{\partial p_f}{\partial y}+\frac{\mu_{nf}}{\rho_{nf}}\left(\frac{\partial^2 v_f}{\partial x^2}+\frac{\partial^2 v_f}{\partial y^2}\right)+g\beta_{nf}\left(T_f-T_c\right), \tag{3}$$

$$u_f\frac{\partial T_f}{\partial x}+v_f\frac{\partial T_f}{\partial y}=\alpha_{nf}\left(\frac{\partial^2 T_f}{\partial x^2}+\frac{\partial^2 T_f}{\partial y^2}\right). \tag{4}$$

Subscript nf represents the nanofluid, and symbol g is gravity acceleration. T_f is the fluid temperature in the clear-fluid part. The variables $(u_f,\ v_f)$ are the fluid velocities in the clear-fluid part. Symbols g is the acceleration due to gravity, $\mu_{nf},\ \rho_{nf},\ \beta_{nf}$ and α_{nf} are dynamic viscosity, the density, thermal expansion and thermal diffusivity of the nanofluids, respectively. The thermophysical properties of the materials used in this work are shown in Table 1.

The fluid flow and energy equation of the porous layer using the Brinkman–Forchheimer model are as follows:

$$\frac{\partial u_p}{\partial x}+\frac{\partial v_p}{\partial y}=0, \tag{5}$$

$$\frac{u_p}{\epsilon^2}\frac{\partial u_p}{\partial x}+\frac{v_p}{\epsilon^2}\frac{\partial u_p}{\partial y}=-\frac{1}{\rho_{nf}}\frac{\partial p_p}{\partial x}+\frac{\mu_{nf}}{\rho_{nf}}\left(\frac{\partial^2 u_p}{\partial x^2}+\frac{\partial^2 u_p}{\partial y^2}\right)-\frac{\nu}{K}u_p-\frac{C_F}{\sqrt{K}}\frac{\sqrt{u_p^2+v_p^2}}{\epsilon^{3/2}}u_p, \tag{6}$$

$$\frac{u_p}{\epsilon^2}\frac{\partial v_p}{\partial x}+\frac{v_p}{\epsilon^2}\frac{\partial v_p}{\partial y}=-\frac{1}{\rho_{nf}}\frac{\partial p_p}{\partial y}+\frac{\mu_{nf}}{\rho_{nf}}\left(\frac{\partial^2 v_p}{\partial x^2}+\frac{\partial^2 v_p}{\partial y^2}\right)+g\beta_{nf}\left(T_p-T_c\right)-\frac{\nu}{K}v_p-\frac{C_F}{\sqrt{K}}\frac{\sqrt{u_p^2+v_p^2}}{\epsilon^{3/2}}v_p, \tag{7}$$

$$u\frac{\partial T_p}{\partial x}+v\frac{\partial T_p}{\partial y}=\alpha_m\left(\frac{\partial^2 T_p}{\partial x^2}+\frac{\partial^2 T_p}{\partial y^2}\right), \tag{8}$$

where T_p is the fluid temperature in the porous layer. The variables $(u_p,\ v_p)$ are the fluid velocities in the porous layer. The thermal diffusivity of a solid matrix is α_m, ϵ is the porosity, K is the porous permeability, and $C_F=1.75/\sqrt{150}$ is the Forchheimer coefficient. The boundary conditions are as follows:

$$u_p=v_p=0,\quad \frac{\partial T_p}{\partial y}=0 \ \text{ on the bottom and top walls enclosure I,} \tag{9}$$

$$u_f=v_f=0,\quad \frac{\partial T_f}{\partial y}=0 \ \text{ on the bottom and top walls enclosure II,} \tag{10}$$

$$u_p = v_p = 0, \quad T_p = T_h, \quad \text{on the left enclosure I,} \tag{11}$$

$$u_f = v_f = 0, \quad T_f = T_h, \quad \text{on the left enclosure II,} \tag{12}$$

$$u_p = v_p = 0, \quad T_p = T_c, \quad \text{on the right enclosure I,} \tag{13}$$

$$u_f = v_f = 0, \quad T_f = T_c, \quad \text{on the right enclosure II,} \tag{14}$$

$$u_f = u_p, \quad v_f = v_p, \quad T_f = T_p,$$
$$\frac{\partial u_f}{\partial x} = \frac{\partial u_p}{\partial x}, \quad \frac{\partial v_f}{\partial x} = \frac{\partial v_p}{\partial x}, \quad k_f \frac{\partial T_f}{\partial x} = k_p \frac{\partial T_p}{\partial x} \quad \text{on the all interfaces,} \tag{15}$$

where the density of the nanofluids suspension, ρ_{nf}, is given as follows:

$$\rho_{nf} = (1 - \phi)\rho_{bf} + \phi\rho_{sp}, \tag{16}$$

where ϕ is the solid volume fraction or concentration of nanoparticles suspended in the host. The thermal diffusivity of the nanofluids is defined by the following:

$$\alpha_{nf} = \frac{k_{nf}}{(\rho Cp)_{nf}}, \tag{17}$$

where the effective heat capacity of the suspension is evaluated as follows:

$$(\rho Cp)_{nf} = (1 - \phi)(\rho Cp)_{bf} + \phi(\rho Cp)_{sp}. \tag{18}$$

The thermal expansion coefficient of the suspension can be evaluated by the following:

$$\beta_{nf} = (1 - \phi)(\beta)_{bf} + \phi\beta_{sp}. \tag{19}$$

The dynamic viscosity of the suspension in this context is as follows:

$$\mu_{nf} = (1 - \phi)^{-5/2}/\mu_{bf} \tag{20}$$

The effective thermal conductivity of the suspension is estimated by the following formula:

$$k_{nf} = \frac{\left[k_{sp} + 2k_{bf} - 2\phi\left(k_{bf} - k_{sp}\right)\right]k_{bf}}{k_{sp} + 2k_{bf} + \phi\left(k_{bf} - k_{sp}\right)}. \tag{21}$$

The governing equations given above are in terms of the so-called primitive variables, i.e., velocity, temperature, and pressure. The solution procedure discussed in this work is based on equations involving the streamfunction, ψ_f, the vorticity, ω_f, and the temperature, T, as variables which are defined as $u = \partial\psi_f/\partial y$, $v = -\partial\psi_f/\partial x$, and $\omega_f = (\partial v_f/\partial x) - (\partial u_f/\partial y)$. The streamfunction satisfies the continuity equation. The vorticity equation is obtained by eliminating the pressure between the two momentum equations, i.e., by taking y-derivative of the first momentum and subtracting from it the x-derivative of the second momentum. This gives the following:

$$\frac{\partial\psi_f}{\partial y}\frac{\partial\omega_f}{\partial x} - \frac{\partial\psi_f}{\partial x}\frac{\partial\omega_f}{\partial y} = \nu_{nf}\left(\frac{\partial^2\omega_f}{\partial x^2} + \frac{\partial^2\omega_f}{\partial y^2}\right) - \beta_{nf}g\left(\frac{\partial T_f}{\partial x}\right), \tag{22}$$

$$\frac{\partial\psi_f}{\partial y}\frac{\partial T_f}{\partial x} - \frac{\partial\psi_f}{\partial x}\frac{\partial T_f}{\partial y} = \alpha_{nf}\left(\frac{\partial^2 T_f}{\partial x^2} + \frac{\partial^2 T_f}{\partial y^2}\right), \tag{23}$$

$$\frac{\partial^2\psi_f}{\partial x^2} + \frac{\partial^2\psi_f}{\partial y^2} = -\omega_f. \tag{24}$$

The momentum and energy equations of the porous part in terms of streamfunction-vorticity formulation are as follows:

$$\frac{\partial\psi_p}{\partial y}\frac{\partial\omega_p}{\partial x} - \frac{\partial\psi_p}{\partial x}\frac{\partial\omega_p}{\partial y} = \nu_{nf}\left(\frac{\partial^2\omega_p}{\partial x^2} + \frac{\partial^2\omega_p}{\partial y^2}\right) - \beta_{nf}g\left(\frac{\partial T_p}{\partial x}\right), \tag{25}$$

$$\frac{\partial\psi_p}{\partial y}\frac{\partial T_p}{\partial x} - \frac{\partial\psi_p}{\partial x}\frac{\partial T_p}{\partial y} = \alpha_{nf}\left(\frac{\partial^2 T_p}{\partial x^2} + \frac{\partial^2 T_p}{\partial y^2}\right), \tag{26}$$

$$\frac{\partial^2\psi_p}{\partial x^2} + \frac{\partial^2\psi_p}{\partial y^2} = -\omega_p. \tag{27}$$

The following nondimensional variables are introduced:

$$\begin{aligned} X &= \frac{x}{L}, \; Y = \frac{y}{L}, \; \Omega = \frac{\omega L^2}{\alpha_{bf}}, \; \Psi = \frac{\psi}{\alpha_{bf}}, \\ S &= \frac{s}{L}, \; \Theta_f = \frac{T_f - T_c}{T_h - T_c}, \; \Theta_p = \frac{T_f - T_c}{T_h - T_c}, \\ Da &= \frac{K}{L^2}, \; Pr_{bf} = \frac{\nu_{bf}}{\alpha_{bf}}, \; Ra_{bf} = \frac{g\beta_{bf}(T_h - T_c)L^3 Pr_{bf}}{\nu_{bf}^2}. \end{aligned} \tag{28}$$

By using the dimensionless parameters, the equations now become the following:

$$\frac{\partial\Psi_f}{\partial Y}\frac{\partial\Omega_f}{\partial X} - \frac{\partial\Psi_f}{\partial X}\frac{\partial\Omega_f}{\partial Y} = \left[\frac{Pr_{bf}}{(1-\phi)^{0.25}\left((1-\phi) + \phi\frac{\rho_{sp}}{\rho_{bf}}\right)}\right]\left(\frac{\partial^2\Omega_f}{\partial X^2} + \frac{\partial^2\Omega_f}{\partial Y^2}\right) + Ra_{bf}Pr_{bf}\left[(1-\phi) + \phi\frac{\beta_{sp}}{\beta_{bf}}\right]\left(\frac{\partial\Theta_f}{\partial X}\right), \tag{29}$$

$$\frac{\partial \Psi_f}{\partial Y}\frac{\partial \Theta_f}{\partial X}-\frac{\partial \Psi_f}{\partial X}\frac{\partial \Theta_f}{\partial Y}=\left[\frac{\frac{k_{nf}}{k_{bf}}}{(1-\phi)+\phi\frac{(\rho Cp)_{sp}}{(\rho Cp)_{bf}}}\right]\left(\frac{\partial^2\Theta_f}{\partial X^2}+\frac{\partial^2\Theta_f}{\partial Y^2}\right), \tag{30}$$

$$\frac{\partial^2 \Psi_f}{\partial X^2}+\frac{\partial^2 \Psi_f}{\partial Y^2}=-\Omega_f. \tag{31}$$

The dimensionless momentum and energy equations of the porous part in terms of streamfunction-vorticity formulation are as follows:

$$\begin{aligned}\frac{\partial \Psi_p}{\partial Y}\frac{\partial \Omega_p}{\partial X}-\frac{\partial \Psi_p}{\partial X}\frac{\partial \Omega_p}{\partial Y}=&\left[\frac{\epsilon Pr_{bf}}{(1-\phi)^{0.25}\left((1-\phi)+\phi\frac{\rho_{sp}}{\rho_{bf}}\right)}\right]\left(\frac{\partial^2\Omega_p}{\partial X^2}+\frac{\partial^2\Omega_p}{\partial Y^2}\right)\\&-\left[\frac{\epsilon^2 Pr_{bf}}{(1-\phi)^{0.25}\left((1-\phi)+\phi\frac{\rho_{sp}}{\rho_{bf}}\right)}\right]\frac{\Omega_p}{Da}\\&+\left[\frac{\epsilon^2 Pr_{bf}}{(1-\phi)^{0.25}\left((1-\phi)+\phi\frac{\rho_{sp}}{\rho_{bf}}\right)}\right]\frac{C_F\sqrt{\left(\frac{\partial \Psi_p}{\partial Y}\right)^2+\left(\frac{\partial \Psi_p}{\partial X}\right)^2}}{\sqrt{Da}}\Omega_p\\&+\epsilon^2 Ra_{bf}Pr_{bf}\left[(1-\phi)+\phi\frac{\beta_{sp}}{\beta_{bf}}\right]\left(\frac{\partial \Theta_p}{\partial X}\right),\end{aligned} \tag{32}$$

$$\frac{\partial \Psi_p}{\partial Y}\frac{\partial \Theta_p}{\partial X}-\frac{\partial \Psi_p}{\partial X}\frac{\partial \Theta_p}{\partial Y}=\left[\frac{\frac{k_{nf}}{k_{bf}}}{(1-\phi)+\phi\frac{(\rho Cp)_{sp}}{(\rho Cp)_{bf}}}\right]\left(\frac{\partial^2\Theta_p}{\partial X^2}+\frac{\partial^2\Theta_p}{\partial Y^2}\right), \tag{33}$$

$$\frac{\partial^2 \Psi_p}{\partial X^2}+\frac{\partial^2 \Psi_p}{\partial Y^2}=-\Omega_p\ . \tag{34}$$

The nondimensional velocity values are zero in the walls. The boundary conditions for the nondimensional temperatures on the outside walls of both enclosures are as follows:

$$\Theta(0,Y)=1;\ \Theta(1,Y)=0\ , \tag{35}$$

$$\frac{\partial \Theta(X,0)}{\partial Y}=\frac{\partial \Theta(X,1)}{\partial Y}=0\ . \tag{36}$$

The continuity of the heat flux at the solid–fluid interfaces in both enclosures is as follows:

$$\frac{\partial \Theta_f}{\partial Y}=R_k\frac{\partial \Theta_p}{\partial Y}, \tag{37}$$

where $R_k=k_p/k_f$ is the thermal conductivity ratio. At the same time, the continuity of the temperature at the solid–fluid interfaces is represented by the following:

$$\Theta_f=\Theta_p. \tag{38}$$

The heat transfer rate across the enclosure is an important parameter in heat transfer applications. The total heat transfer rate in terms of the average Nusselt number, $(\overline{Nu})$ at the solid–fluid interfaces is defined as follows:

$$\overline{Nu}=\frac{k_{nf}}{k_{bf}}\int_0^1-\frac{\partial \Theta}{\partial X}dY. \tag{39}$$

3. Numerical Method and Validation

An iterative finite difference procedure is employed to solve Equations (29)–(34) subject to the boundary conditions Equations (35)–(38). The numerical solution will be preceded by giving the finite difference equation (FDE) of the streamfunction equation for the bounded enclosure and the partitioned enclosure. The FDE of the streamfunction written in the Gaussian SOR formulation is as follows:

$$\begin{aligned}\Psi_{i,j}^{k+1}=&\Psi_{i,j}^{k}+\frac{\lambda_r}{2\left(1+\left(\frac{\Delta X}{\Delta Y}\right)^2\right)}\left[\Psi_{i+1,j}^{k}+\Psi_{i-1,j}^{k+1}\right.\\&+\left(\frac{\Delta X}{\Delta Y}\right)^2\left(\Psi_{i,j+1}^{k}+\Psi_{i,j-1}^{k+1}\right)\\&\left.-2\left(1+\left(\frac{\Delta X}{\Delta Y}\right)^2\right)\Psi_{i,j}^{k}+(\Delta X)^2\left(-\Omega_{i,j}\right)^k\right].\end{aligned} \tag{40}$$

The FDE of vorticity and energy in the clear fluid and porous fractions could be written in the same way. The grid-points distribution at the porous layer and clear-fluid layer is shown in Figure 2, where $NS+1$ is the number of nodal points in the horizontal axis inside the porous layer. Following this setting then, the conditions at the fluid-porous interface are:

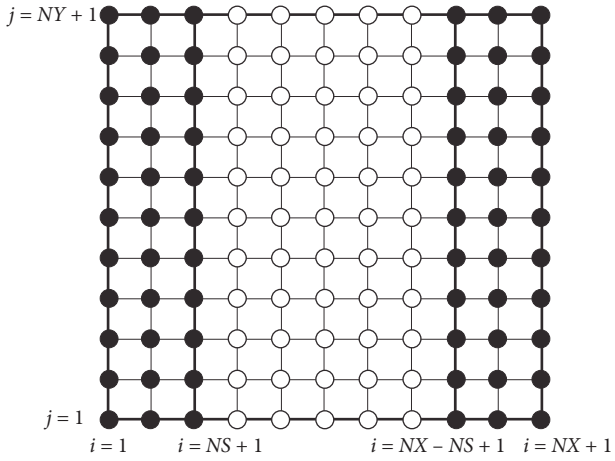

Figure 2: Grid-points distribution in the porous layer ($j \le NS+1$, $j \ge NX-NS+1$) and clear-fluid layer ($j \ge NS+1, j \le NX-NS+1$).

$$\begin{aligned}\left(\Theta_p\right)_{i,j}^{k+1} &= \left(\Theta_f\right)_{i,j}^{k}\\ \left(\Theta_p\right)_{i,j}^{k+1} &= \left[\left(\frac{1}{R_k}\right)\left(-\left(\Theta_f\right)_{i,j+2}^{k}\right.\right.\\ &\quad + 4\left(\Theta_f\right)_{i,j+1}^{k} - 3\left(\Theta_f\right)_{i,j}^{k}\Big)\\ &\quad \left. + 4\left(\Theta_f\right)_{i,j-1}^{k} - \left(\Theta_f\right)_{i,j-1}^{k}\right]/3.\end{aligned} \tag{41}$$

The conditions at the fluid-porous interface for enclosure II could be written in the same way.

The upwind scheme was employed to ensure solution stability when addressing the convective terms in the momentum and energy equations. An accurate formula of the second order is used to establish the boundary condition for the vorticity. As an illustration, the vorticity along the porous ($1 \le i \le NS+1$ and $NX-NS+1 \le i \le NX+1$) and fluid ($NS+1 \le i \le NX-NS+1$) part is represented as follows:

$$\Omega = -\frac{\left(8\Psi_{1,j} - \Psi_{2,j}\right)}{2\left(\Delta Y^2\right)}. \tag{42}$$

Similar expressions can be written for other walls as well. The conditions on the interfaces are as follows:

$$\Omega = \frac{4\Omega_f(i+1,j) - \Omega_f(i+2,j) + 4\Omega_p(i-1,j) - \Omega_p(i-2,j)}{6}. \tag{43}$$

Regular and uniform grid distribution is used for the whole enclosure. The effect of grid resolution was examined in order to select the appropriate grid density, as demonstrated in Table 2 for $S = 0.3$, $Da = 10^{-4}$, $R_k = 2$, and $\phi = 0.05$. The data indicate that a 111×111 grid can be used in the final computations. Verification of the current streamlines and isotherms was made against that of Beckermann et al. [5] when the porous layer is attached on the right part at $Ra = 3.028 \times 10^7$, $Da = 1.296 \times 10^{-5}$, $Pr = 6.97$, $R_k = 1.383$, and $S = 0.5$ (see Figure 3). Thus, it is decided that the present code is valid for further calculations.

Table 2: Grid sensitivity check for the enclosure I and enclosure II at $S = 0.3$, $Da = 10^{-4}$, $R_k = 2$, and $\phi = 0.05$.

Grid size	$\overline{Nu}_{\mathrm{I}}$	$\overline{Nu}_{\mathrm{II}}$
21×21	2.4953	6.2870
31×31	2.5023	6.2710
41×41	2.5051	6.2646
51×51	2.5066	6.2611
61×61	2.5074	6.2590
71×71	2.5080	6.2579
81×81	2.5283	6.2139
91×91	2.5287	6.2134
101×101	2.5288	6.2128
111×111	2.5487	6.1706
121×121	2.5485	6.1705

4. Results and Discussion

The analysis in the undergoing numerical investigation is performed in the following range of the associated dimensionless groups: the thickness of the porous medium, $0 \le S \le 1$, the nanoparticles volume fraction ($0.0 \le \phi \le 0.05$), the thermal conductivity ratio ($0.5 \le R_k \le 10$), and the Darcy number ($10^{-5} \le Da \le 10^{-2}$). The Prandtl number value and the Rayleigh number value are fixed at $Pr = 4.62$ and $Ra = 10^6$. Here, the Rayleigh number, $Ra = 10^6$ to keep the convection in the laminar regime and the applicability of Boussinesq approximation. The Darcy number, $10^{-5} \le Da \le 10^{-2}$ to cover a pore-level in the Darcy and non-Darcy models. The nanoparticles concentration ($0.0 \le \phi \le 0.05$) is an optimal range of volume fraction for alumina nanomaterials where the rate of thermal transfer is maximized. Beyond this optimal range, an excessive concentration of nanoparticles can lead to aggregation or other negative effects, which might reduce the heat transfer performance. The flow and temperature distribution are presented in terms of streamlines and isotherms. The heat transfer rate is presented by the average Nusselt number.

Figure 4 depicts the effects of the porous thickness for enclosure I and enclosure II on the streamlines for $Da = 10^{-4}$, $R_k = 2$, and $\phi = 0.05$. Without a porous layer ($S = 0.0$), a skewed and stretched vortex is found in the center of the enclosure. The eye of the vortex in the first enclosure becomes a circled one as porous thickness increases, and later, the eye is elongated vertically. The eye of the vortex in the hot part of the second enclosure is found in the lower portion, while the eye in the cold part is found in the upper portion of the enclosure. The reduction in vortex strength for both enclosures indicates the influence of the porous layer thickness. The circulation strength in the second enclosure is higher than that in the first enclosure for the same porous thickness. This attributes to the convective flow by heating the left wall in the enclosure I is retarded by the porous layer. Figure 4 also shows the spatial displacement and changing of

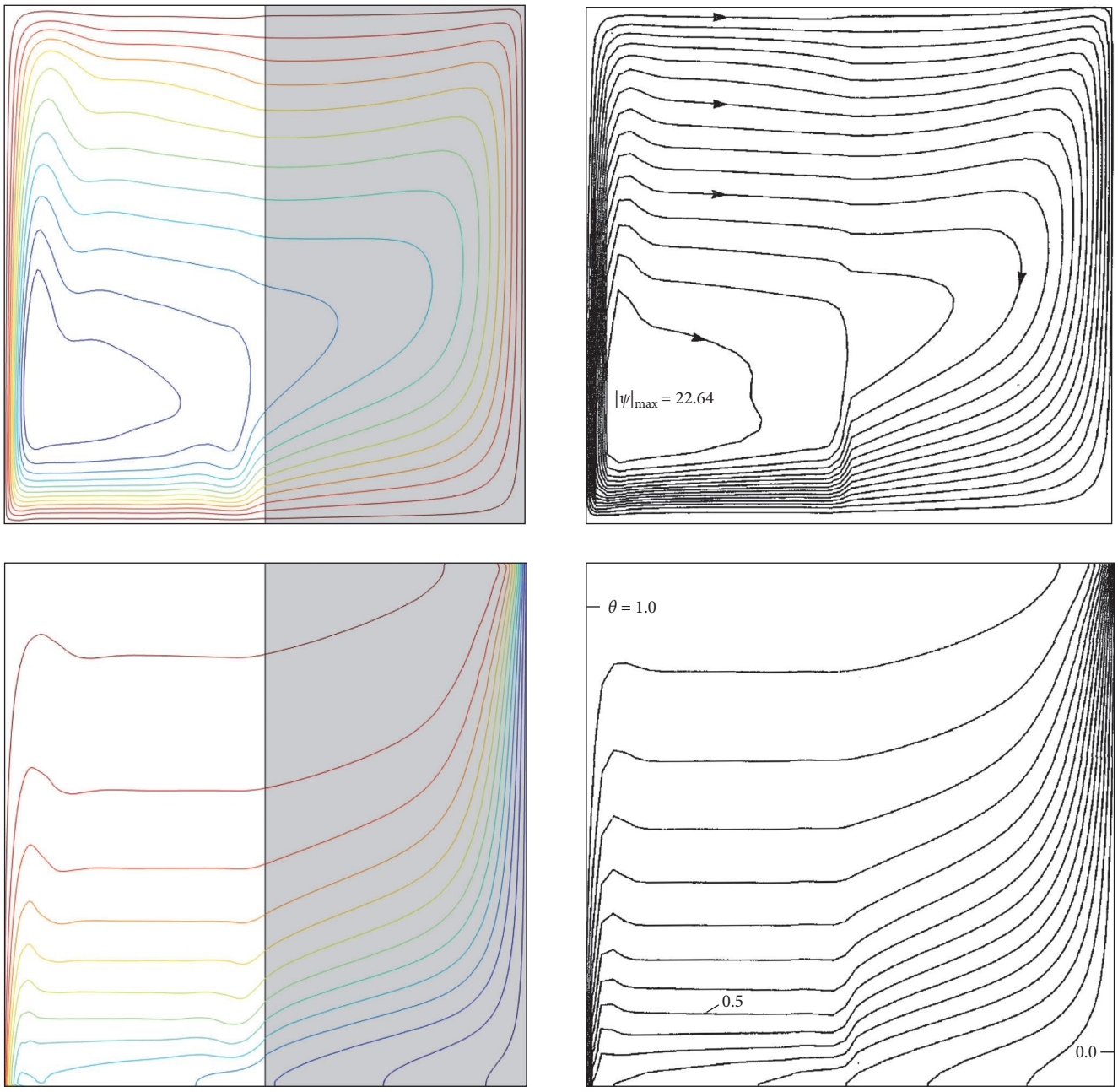

FIGURE 3: Comparison of the current streamlines and isotherms (left) against that of Beckermann et al. [5] when the porous layer is attached on the right at $Ra = 3.028 \times 10^7$, $Da = 1.296 \times 10^{-5}$, $Pr = 6.97$, $R_k = 1.383$, and $S = 0.5$.

the core vortex of the convective cells by varying the porous size. Almost double eyes are created in the enclosure without a porous layer. There is more intensive nanofluid motion in the clear-nanofluid case owing to the direct nanofluid heating of the left layer and no obstruction in the middle for flow movement.

Figure 5 depicts the effects of the porous thickness for enclosure I (left) and enclosure II (right) at $Da = 10^{-4}$, $R_k = 2$, and $\phi = 0.05$. When there is no porous layer ($S = 0$), the warm nanofluid rises and moves away from the heated surface, leading to heat loss to the surrounding walls. Consequently, the nanofluid cools, becomes denser, and descends back toward the heat source, resulting in distorted isotherms. These isotherms are more widely spaced near the heated surface. In enclosure I, some of the heat released from the hot surface crosses the porous wall and travels with the nanofluid in the center. As the nanofluid approaches the cold wall, some of the heat flow is terminated, while the rest reaches the lower part of the cold wall. As the cold nanofluid sweeps the lower wall, the direction of the heat flow is reversed. Enclosure II exhibits a similar behavior, where some of the heat released by the hot surface travels with the nanofluid and crosses the porous partition, reaching the cold surface. Subsequently, some of this heat is reversed, but to a

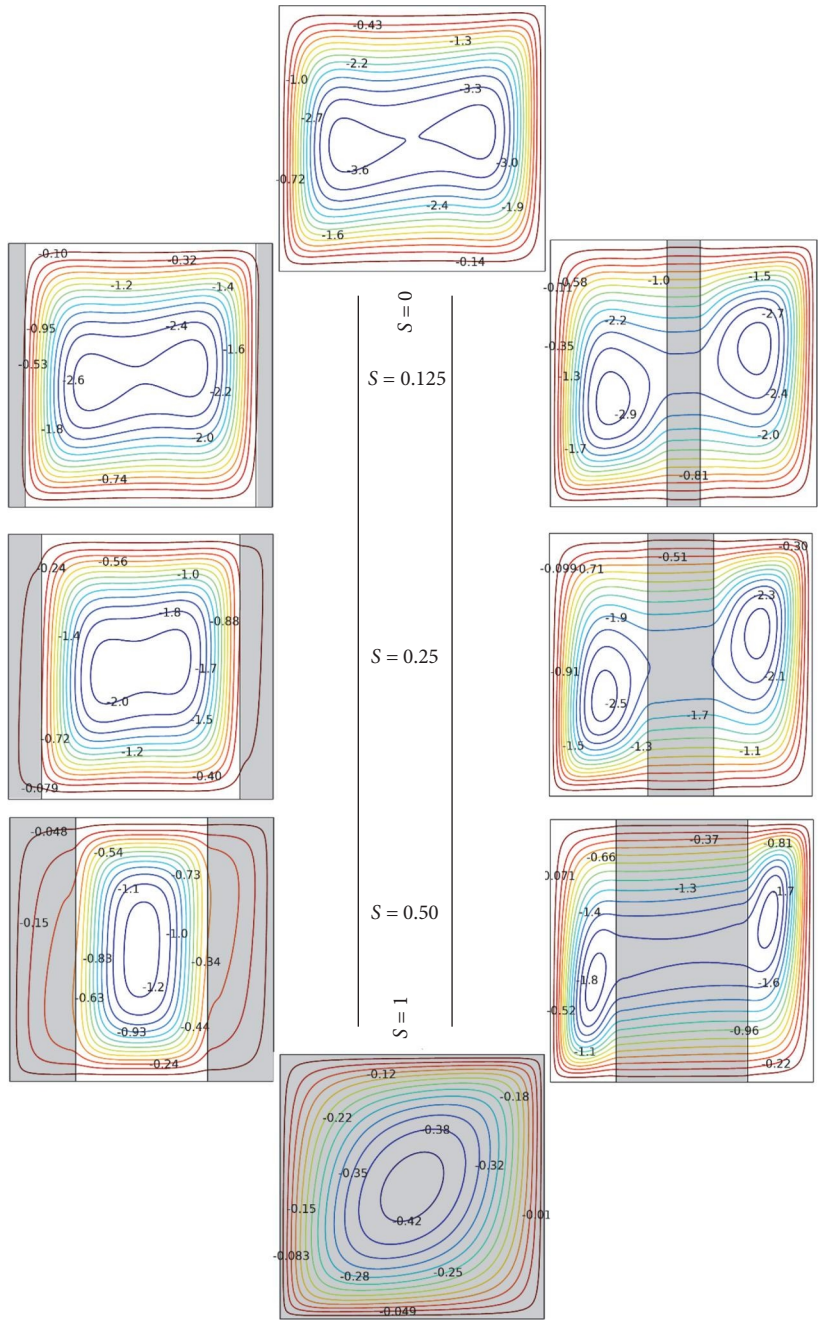

FIGURE 4: Streamlines evolutions by varying porous thickness for enclosure I (left) and enclosure II (right) at $Da = 10^{-4}$, $R_k = 2$, and $\phi = 0.05$.

lesser extent compared to enclosure I. Increasing the porous thickness in both enclosures results in less distortion of the isotherms. The isotherms become more closely packed, indicating a decrease in the temperature gradient. The heat in the enclosure I is conducted almost vertically across all porous thicknesses. The heat in enclosure II is predominantly conducted in a nearly vertical direction across all porous thicknesses.

Figure 6 provides a visual representation of the flow fields and thermal distribution within enclosure I, highlighting the effect of the Darcy number while maintaining constant values of $S = 0.5$, $R_k = 2$, and $\phi = 0.05$. The strength of the flow initially decreases and then increases as the Darcy number increases. In the Darcy regime ($Da = 10^{-5}$), no flow circulation cells are formed on both porous sides. The eye flow takes on an elliptical shape, elongated vertically. However, as the Darcy number increases, the elliptical shape is compressed. At $Da = 10^{-5}$ and $Da = 10^{-4}$, the isotherms within the porous layers appear almost parallel to the hot and cold surfaces. However, at $Da = 10^{-2}$, the isotherms within the porous layers are distorted. These observations can be attributed to the interplay between the Darcy number, the streamline penetration within the porous sides, and the fluid side. Increasing the Darcy number reduces the drag within the

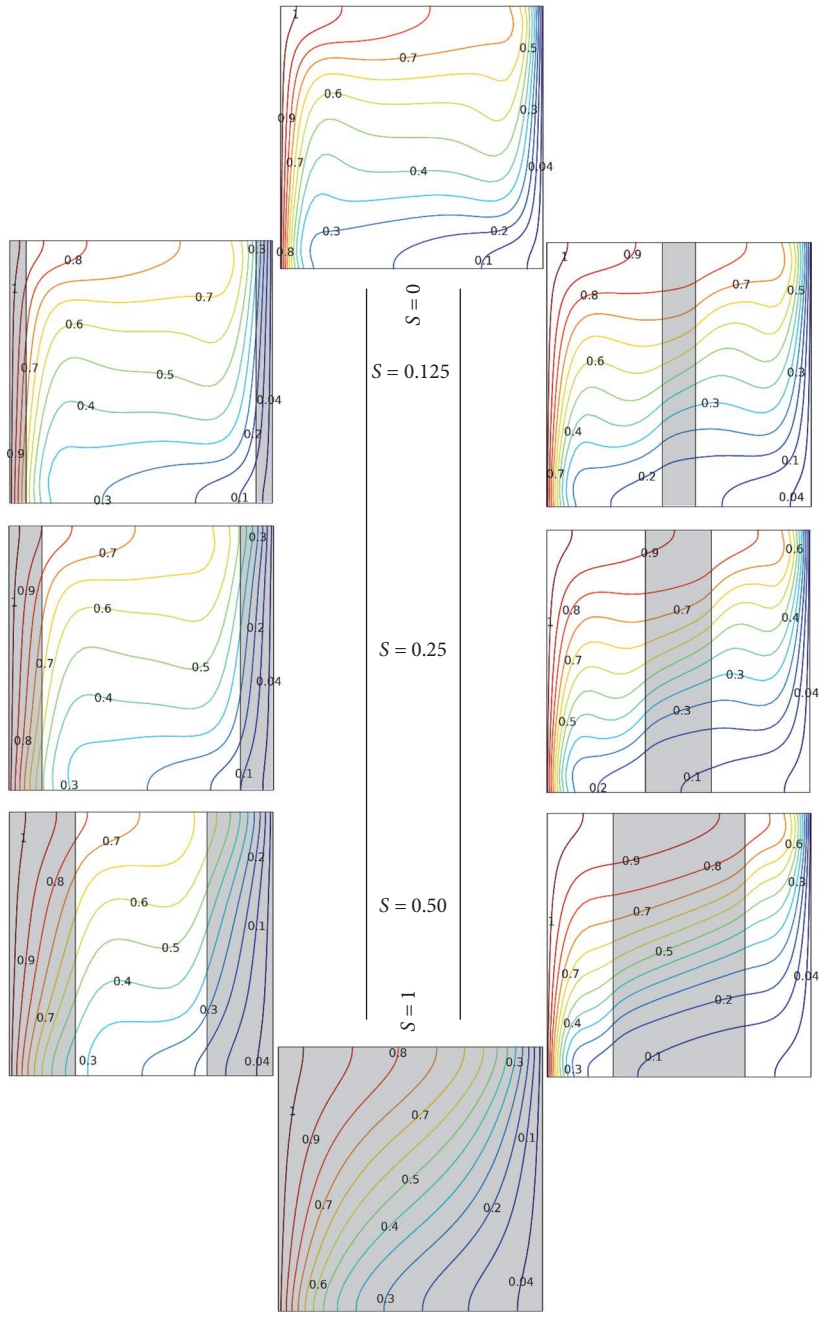

FIGURE 5: Isotherms evolutions by varying porous thickness for enclosure I (left) and enclosure II (right) at $Da = 10^{-4}$, $R_k = 2$, and $\phi = 0.05$.

porous layers, allowing for increased streamline penetration and resulting in distorted isotherms. The streamlines and isotherms exhibit symmetry with respect to the midplane that equally divides the heated and cooled sections. This symmetry suggests equal fluid velocities as the fluid rises in the left layer and reverses in the right layer, indicating a balanced convective flow.

Figure 7 illustrates the streamlines and isotherms, providing insight into the influence of the Darcy number on the flow fields and thermal distribution within enclosure II, while keeping $S = 0.5$, $R_k = 2$, and $\phi = 0.05$ constant. Two distinct eye circulations can be observed at Darcy numbers, $Da = 10^{-5}$ and $Da = 10^{-4}$. In the hot portion, the eye flow exhibits a counter-clockwise direction, while in the cold portion, it follows a clockwise direction. The eye flow of the hot partition predominantly occurs in the lower part, while the eye flow of the cold partition is observed in the upper part. As the Darcy number increases to $Da = 10^{-2}$, the eye flows of the cold and hot partitions merge into a single flow. This unified flow conducts heat more intensively from the hot fluid, benefiting from the higher permeability of the enclosure. Conversely, at low permeability values, the isotherms within the partition appear almost parallel to the hot and cold surfaces, indicating that the

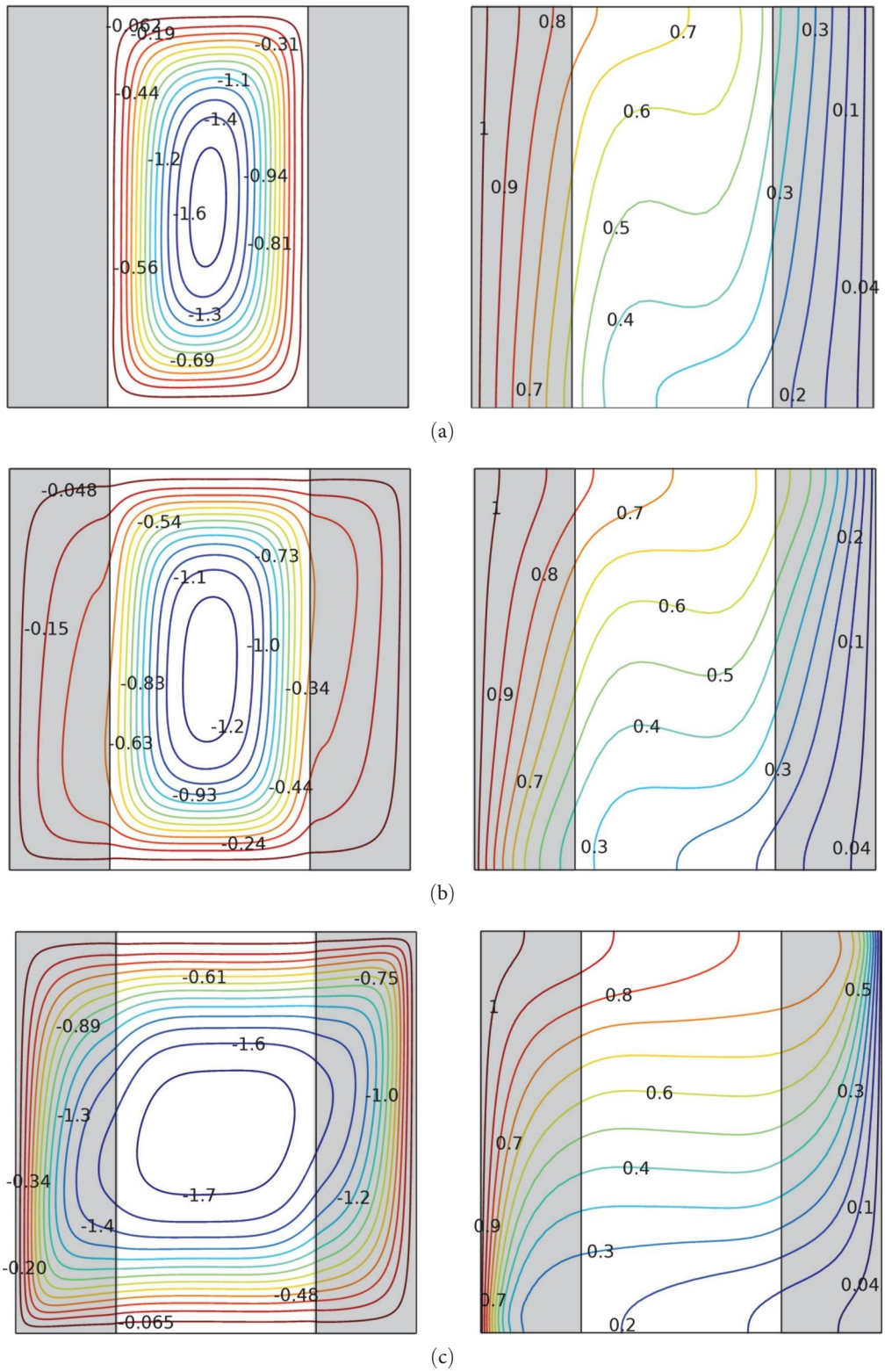

FIGURE 6: Streamlines (left) and isotherms (right) evolutions for several Darcy number of the enclosure I at $S = 0.5$, $R_k = 2$, and $\phi = 0.05$: (a) $Da = 10^{-5}$; (b) $Da = 10^{-4}$; (c) $Da = 10^{-2}$.

partition acts as a thermal barrier, impeding heat transfer between the two sides. However, at higher permeability values, the isotherms within the partition become distorted, indicating that the porous part functions as an additional heat-conducting channel, facilitating heat transfer between the hot and cold regions [29].

Figure 8 illustrates the variations in the average Nusselt number for both enclosures as a function of the porous

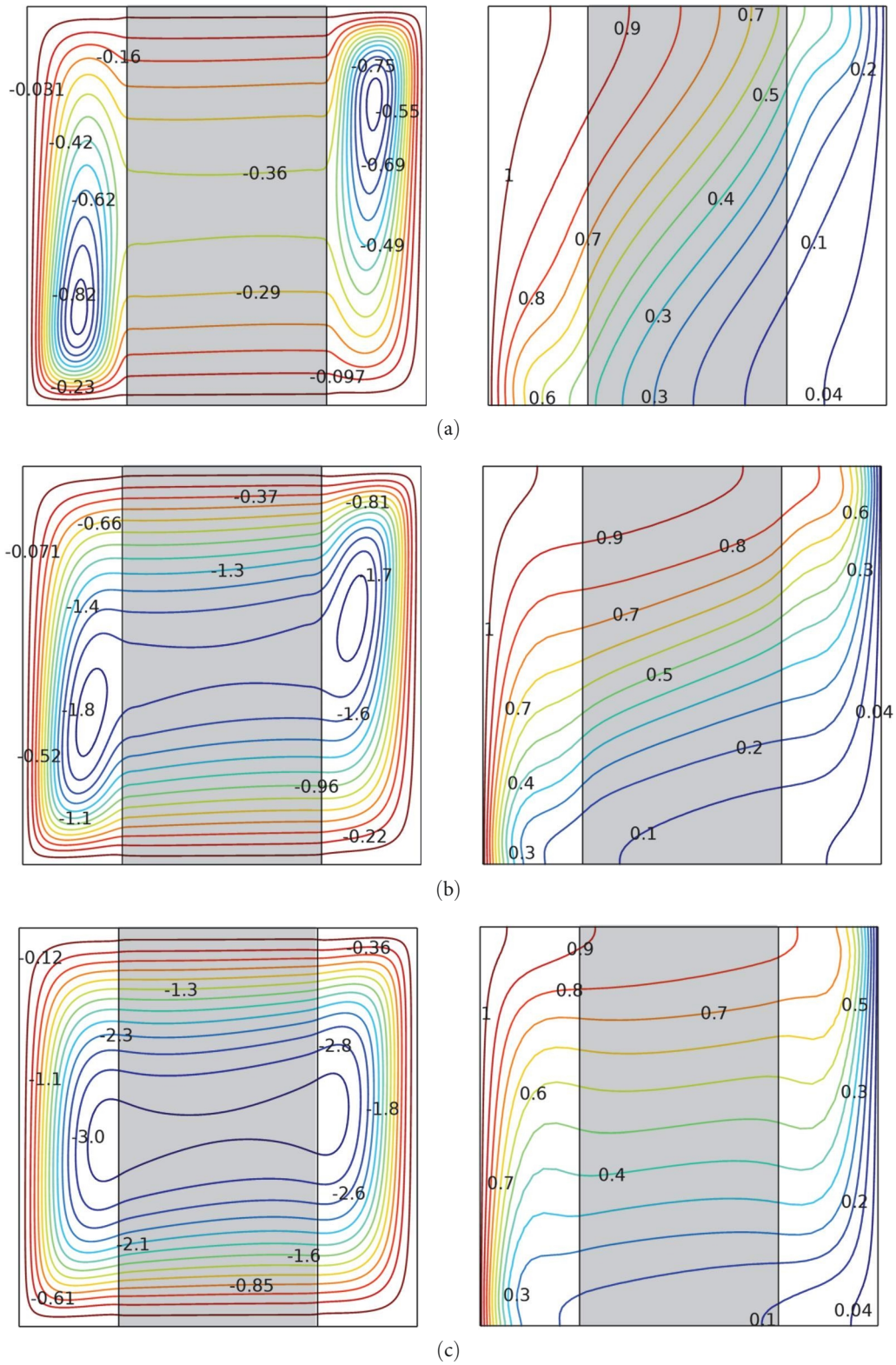

FIGURE 7: Streamlines (left) and isotherms (right) evolutions for several Darcy number of the enclosure II at $S = 0.5$, $R_k = 2$, and $\phi = 0.05$: (a) $Da = 10^{-5}$; (b) $Da = 10^{-4}$; (c) $Da = 10^{-2}$.

thickness, while maintaining a constant value of $R_k = 2$ and $\phi = 0.05$ and considering different values of S. It can be observed that the average Nusselt number decreases with increasing porous thickness for all permeabilities, with the lowest value obtained in the Darcy regime. Interestingly, for the second enclosure, the average Nusselt number remains constant with increasing porous thickness up to $S = 0.75$ when $Da = 10^{-3}$. This phenomenon can be attributed to the

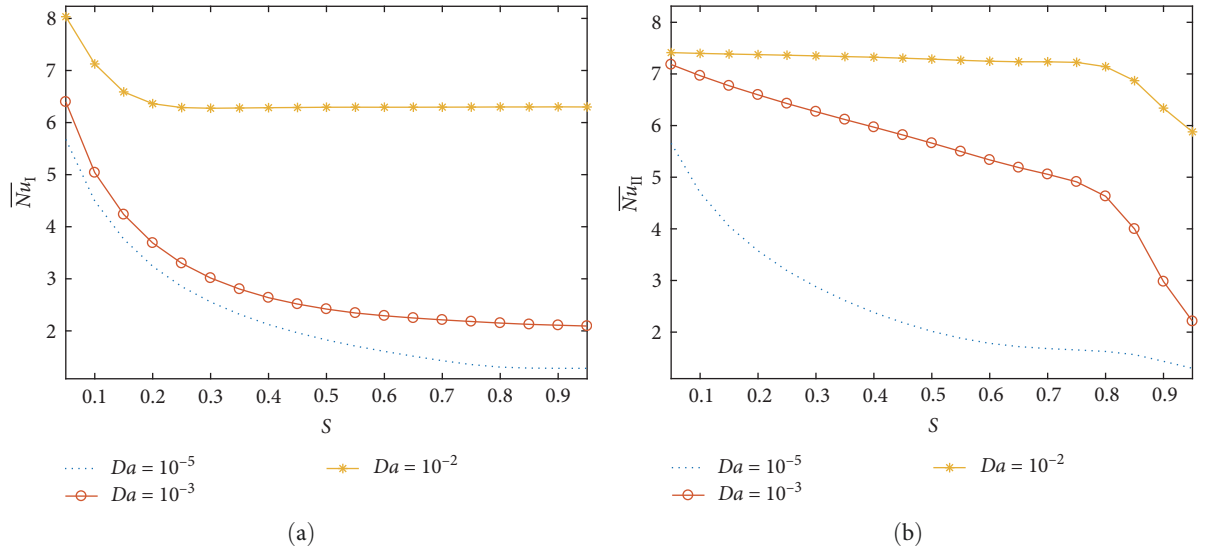

FIGURE 8: Variation of $\overline{Nu}_{\mathrm{I}}$ and $\overline{Nu}_{\mathrm{II}}$ with S for different Da at $R_k = 2$ and $\phi = 0.05$: (a) enclosure I; (b) enclosure II.

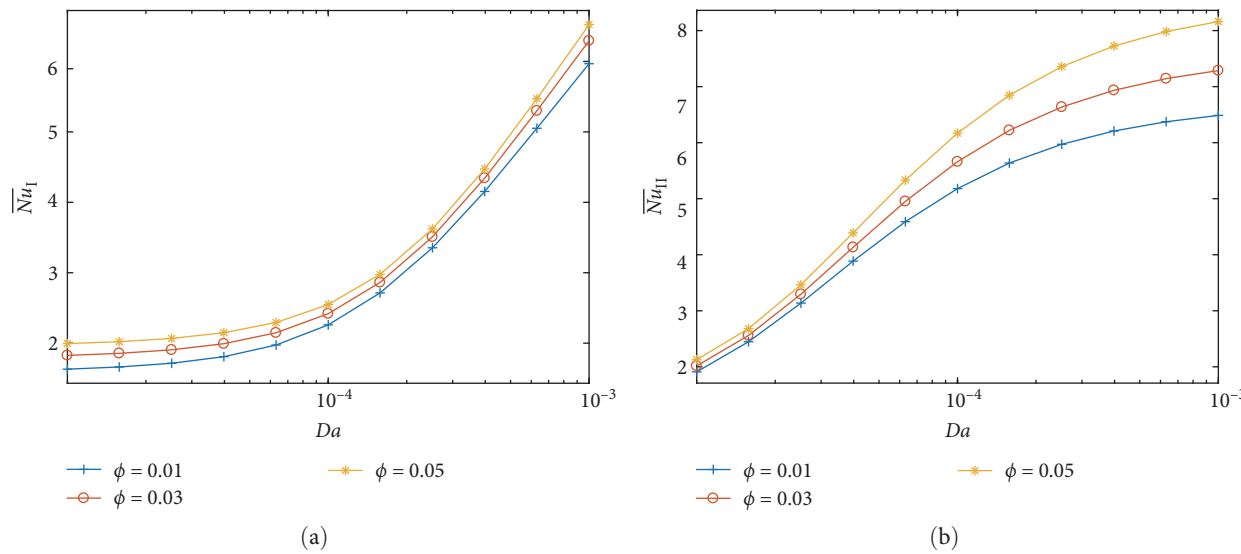

FIGURE 9: Variation of $\overline{Nu}_{\mathrm{I}}$ (a) and $\overline{Nu}_{\mathrm{II}}$ (b) with Da for different ϕ at $R_k = 2$ and $S = 0.5$: (a) enclosure I; (b) enclosure II.

increased drag within the porous layer and the reduced penetration of streamlines with higher S values. As the Darcy number increases, there is less drag and more streamline penetration, leading to enhanced momentum exchange between the two layers. However, in the case of the second enclosure, as the Darcy number continues to increase, a significant number of streamlines pass through the porous partition, which has high heat resistance. This results in a balance between the increased permeability of the porous layer and the heat resistance, ultimately resulting in a constant average Nusselt number.

The variations of the average Nusselt number for enclosure I and enclosure II with respect to the Darcy number are depicted in the upper and lower parts of Figure 9, respectively, while maintaining a constant value of $R_k = 2$ and $S = 0.5$. It is evident that as the Darcy number increases, the average Nusselt number also increases for all concentrations in both enclosures. The profiles of the average Nusselt number exhibit different trends between enclosure I and enclosure II. Initially, as the Darcy number increases, $\overline{Nu}_{\mathrm{I}}$ shows a slow response, but after reaching a sufficiently high Darcy number, the $\overline{Nu}_{\mathrm{I}}$ grows rapidly. Conversely, $\overline{Nu}_{\mathrm{II}}$ shows a rapid response to an increasing Darcy number, but after reaching a sufficiently high value, its growth slows down. Both $\overline{Nu}_{\mathrm{I}}$ and $\overline{Nu}_{\mathrm{II}}$ increase with increasing nanoparticle concentration, with the increase being more pronounced at higher Da values in the case of enclosure II. An augmentation in values of $\overline{Nu}_{\mathrm{I}}$ up to 22% is obtained as concentration is adjusted from 1% to 5%. Similarly, an augmentation in values of $\overline{Nu}_{\mathrm{II}}$ up to 25% is obtained as concentration is adjusted from 1% to 5%. This can be attributed to the significant impact of the solid concentration of nanoparticles at

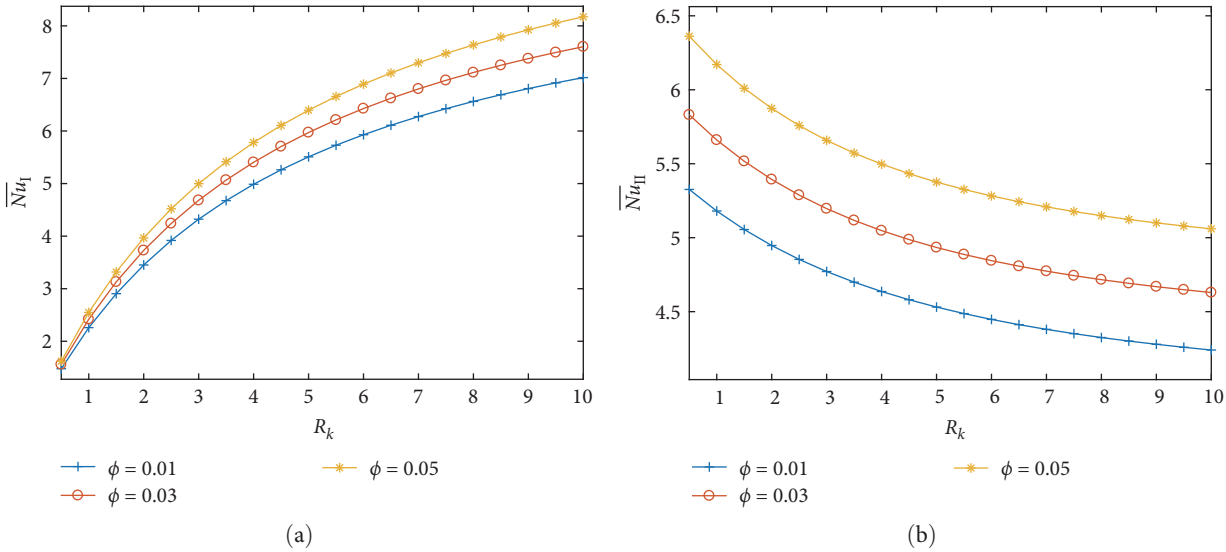

FIGURE 10: Variation of $\overline{Nu}_{\mathrm{I}}$ (a) and $\overline{Nu}_{\mathrm{II}}$ (b) with R_k for different ϕ at $S = 0.5$ and $Da = 10^{-4}$: (a) enclosure I; (b) enclosure II.

TABLE 3: Variations of the average Nusselt number with the Darcy number for various values of the governing parameters.

	R_k	0.5						5.0					
	Da	10^{-5}		10^{-3}		10^{-2}		10^{-5}		10^{-3}		10^{-2}	
ϕ	S	EnI	EnII	EnI	EnII	EnI	EnII	EnI	EnII	EnI	EnII	EnI	EnII
	0.1	2.86	4.32	4.33	6.57	5.29	6.61	5.91	4.27	11.48	6.42	16.25	6.46
	0.3	1.39	2.67	3.86	6.58	5.42	6.68	4.82	3.02	14.28	6.21	26.42	6.35
0.01	0.5	0.94	1.87	3.91	6.58	5.51	6.77	4.13	2.43	14.52	6.01	26.45	6.28
	0.7	0.72	1.48	3.98	6.60	5.60	6.89	3.61	2.64	14.08	5.85	26.10	6.29
	0.9	**0.62**	0.93	4.06	5.53	5.70	6.66	4.04	4.05	13.45	6.40	25.77	8.21
	0.1	3.05	4.50	4.53	7.00	5.55	7.04	6.29	4.48	11.94	6.84	16.93	6.89
	0.3	1.48	2.73	3.98	7.00	5.65	7.12	5.13	3.18	14.67	6.61	27.47	6.76
0.02	0.5	1.00	1.90	4.04	6.99	5.74	7.21	4.40	2.57	14.91	6.38	27.51	6.68
	0.7	0.77	1.50	4.11	7.01	5.83	7.34	3.84	2.81	14.46	6.19	27.12	6.69
	0.9	0.66	0.96	4.19	5.80	5.93	7.05	4.31	4.31	13.79	6.72	26.75	8.70
	0.1	3.22	4.67	4.71	7.42	5.77	7.46	6.66	4.67	12.36	7.25	17.57	7.30
	0.3	1.56	2.79	4.08	7.41	5.84	7.55	5.42	3.34	14.99	6.99	28.36	7.17
0.03	0.5	1.05	1.93	4.14	7.39	5.93	7.64	4.65	2.71	15.23	6.74	28.40	7.08
	0.7	0.81	1.52	4.20	7.39	6.02	7.76	4.06	2.95	14.77	6.52	27.96	7.07
	0.9	0.69	1.00	4.29	6.07	6.12	7.43	4.53	4.54	14.05	7.00	27.56	9.12
	0.1	3.38	4.84	4.88	7.86	5.98	7.91	7.04	4.87	12.78	7.68	18.24	7.74
	0.3	1.63	2.85	4.16	7.84	6.00	7.99	5.72	3.50	15.28	7.40	29.19	7.59
0.04	0.5	1.10	1.96	4.22	7.81	6.09	8.09	4.89	2.84	15.50	7.12	29.19	7.49
	0.7	0.84	1.53	4.29	7.80	6.18	8.20	4.27	3.08	15.02	6.86	28.72	7.46
	0.9	0.72	1.03	4.37	6.34	6.29	7.83	4.72	4.73	14.26	7.26	28.27	9.53
	0.1	3.54	5.03	5.04	8.35	6.19	8.41	7.46	5.10	13.22	8.17	18.96	8.24
	0.3	1.70	2.92	4.24	8.32	6.15	8.49	6.04	3.68	15.56	7.85	**29.99**	8.07
0.05	0.5	1.15	1.99	4.30	8.28	6.24	8.59	5.14	2.99	15.75	7.54	29.95	7.96
	0.7	0.87	1.55	4.36	8.24	6.33	8.69	4.49	3.20	15.24	7.25	29.42	7.91
	0.9	0.74	1.07	4.44	6.66	6.43	8.27	4.91	4.91	14.45	7.52	28.93	9.94

high permeability in the second enclosure. Here, the presence of nanoparticles further enhances heat transfer by promoting thermal conductivity and disrupting the thermal boundary layer, particularly in the case of enclosure II, where the porous layer acts as an additional heat-conducting pathway.

Figure 10 illustrates the variations of the average Nusselt number for enclosure I and enclosure II as a function of the

thermal conductivity ratio (R_k), with a constant value of $S = 0.5$ and $Da = 10^{-4}$. It is observed that both $\overline{Nu}_{\mathrm{I}}$ and $\overline{Nu}_{\mathrm{II}}$ increase with increasing nanoparticle concentration. Figure 10(a) shows that the heat transfer rate increases with the increase of the thermal conductivity ratio, regardless of the nanoparticle concentration. On the contrary, Figure 10(b) demonstrates that the heat transfer rate decreases as the thermal conductivity ratio increases. Moreover, the heat transfer enhancement is more pronounced at higher R_k values for the first enclosure, while it remains constant at a given thermal conductivity ratio value. This behavior can be explained by the fact that in the case of the first enclosure, the porous medium with high conductivity acts as a pathway for heat transfer. In the case of the second enclosure, however, the porous partition acts as a thermal barrier, preventing heat transfer between the two sides despite its high conductivity.

The summary of variations in the average Nusselt number with the Darcy number is presented in Table 3 for different values of the governing parameters. It is worth noting that the labels "EnI" and "EnII" represent enclosure I and enclosure II, respectively. The average Nusselt number of enclosure I exhibits increasing values in accordance with the sequence $R_k = 0.5$ and $R_k = 5.0$. The average Nusselt number of enclosure II exhibits decreasing values in accordance with the sequence $R_k = 0.5$ and $R_k = 5.0$. For all Darcy numbers, the average Nusselt number decreases as the porous thickness increases. With an increase in the Darcy number, the average Nusselt number also enhances for all concentrations in both enclosures. The minimum average Nu occurs at $R_k = 0.5$, $Da = 10^{-5}$, $\phi = 0.01$, and $S = 0.9$ in enclosure I, denoted by the bold value 0.62. Similarly, in enclosure I, the maximum average Nu is observed at $R_k = 5.0$, $Da = 10^{-2}$, $\phi = 0.05$, and $S = 0.3$, with the bold value 29.99.

5. Conclusions

To accurately model the fluid flow and heat transfer phenomena in the composite enclosures, we employ the Navier–Stokes equations to govern the fluid flow within the nanofluid domain. The presence of saturated porous layers requires the use of the Brinkman–Forchheimer extended Darcy model to describe the flow behavior. This combined approach allows us to capture the complex interaction between the fluid flow in the nanofluid layer and the porous structure, providing a comprehensive understanding of the convective heat transfer process in composite enclosures. To solve the governing equations, an iterative finite difference method is employed, which has been proven effective in similar studies and ensures accurate numerical results. In the present numerical simulations, two categories of morphology have been studied, namely the surrounded enclosure and the divided enclosure with different porous fraction. Detailed computational results for fluid flow, temperature distribution, heat path, and heat transfer characteristics in both enclosures were presented in graphical form. The main conclusions of the present analysis are as follows:

(1) The flow patterns within both enclosures are influenced by the configuration of the porous thickness, the permeability value, and the thermal conductivity ratio. The streamlines and isotherms exhibit symmetry with respect to the middle plane of enclosure I, while streamlines and isotherms exhibit symmetry with respect to the diagonal plane of enclosure II.

(2) At very small Darcy numbers, the convective flow generates a vortex only in the nanofluid layer, which subsequently spreads out to the porous layer as the Darcy number increases. However, the vortex persists in the nanofluid layer of both enclosures.

(3) The highest concentration results in the greatest heat transfer for each porous layer configuration, permeability value, and thermal conductivity ratio.

(4) Heat transfer enhancement is more pronounced with higher thermal conductivity ratios in enclosure I, while in enclosure II, it is more pronounced with higher permeability values.

(5) An augmentation in values of $\overline{Nu}_{\mathrm{I}}$ up to 22% is obtained as concentration is adjusted from 1% to 5%. Similarly, an augmentation in values of $\overline{Nu}_{\mathrm{II}}$ up to 25% is obtained as concentration is adjusted from 1% to 5%.

The key findings of this research underscore the practical importance of incorporating porous materials into the design and evaluation of heat transfer systems, as they have a significant impact on the thermal efficiency of both buildings and HVAC systems. However, further research and experimentation are necessary to explore the effects of varying parameters and real-world applications in detail.

Nomenclature

C_F: Forchheimer constant
C_p: Heat capacity
Da: Darcy number
g: Gravitational acceleration
k: Thermal conductivity
K: Permeability
L: Enclosure side
Nu: Nusselt number
Pr: Prandtl number
R_k: Thermal conductivity ratio
S: Porous layer thickness
T: Fluid temperature
x, y: Space coordinates

Greek symbols

β: Coefficient of thermal expansion
ϵ: Porosity
Θ: Dimensionless fluid temperature
Ω: Vorticity
ρ: Density
ϕ: Nanoparticles volume fraction
Ψ: Streamfunction
μ: Dynamic viscosity

Subscript

bf: Basefluids
c: Cold
f: Fluid layer
h: Hot
nf: Nanofluids
p: Porous layer
sp: Solid particles.

Data Availability

The data used to support the findings of this study are available from the corresponding author upon request.

Conflicts of Interest

The author declares that there are no conflicts of interest regarding the publication of this paper.

References

[1] S. U. S. Choi, "Enhancing thermal conductivity of fluids with nanoparticles," *ASME's Fluids Engineering Division*, vol. 231, pp. 99–105, 1995.

[2] G. C. Bourantas, E. D. Skouras, V. C. Loukopoulos, and V. N. Burganos, "Heat transfer and natural convection of nanofluids in porous media," *European Journal of Mechanics—B/Fluids*, vol. 43, pp. 45–56, 2014.

[3] R. A. Mahdi, H. A. Mohammed, K. M. Munisamy, and N. H. Saeid, "Review of convection heat transfer and fluid flow in porous media with nanofluid," *Renewable and Sustainable Energy Reviews*, vol. 41, pp. 715–734, 2015.

[4] H. M. Duwairi, M. Alrbai, and M. B. Al-Dweik, "Performance enhancement of an evacuated tubes solar collector using Forchheimer's saturated porous media with embedded nanofluid," *Advances in Mechanical Engineering*, vol. 14, no. 3, Article ID 2022, 2022.

[5] C. Beckermann, S. Ramdhyani, and R. Viskanta, "Natural convection flow and heat transfer between fluid layer and porous layer inside a rectangular enclosure," *Journal of Heat Transfer*, vol. 109, no. 2, pp. 363–370, 1987.

[6] F. Chen and C. F. Chen, "Convection in superposed fluid and porous layer," *Journal of Fluid Mechanics*, vol. 234, pp. 97–119, 1992.

[7] B. Goyeau, D. Lhuillier, D. Gobin, and M. G. Velarde, "Momentum transport at a fluid–porous interface," *International Journal of Heat and Mass Transfer*, vol. 46, no. 21, pp. 4071–4081, 2003.

[8] X. B. Chen, P. Yu, Y. Sui, S. H. Winoto, and H. T. Low, "Natural convection in a cavity filled with porous layers on the top and bottom walls," *Transport in Porous Media*, vol. 78, no. 2, pp. 259–276, 2009.

[9] A. J. Chamkha and M. A. Ismael, "Natural convection in differentially heated partially porous layered cavities filled with a nanofluid," *Numerical Heat Transfer, Part A: Applications*, vol. 65, no. 11, pp. 1089–1113, 2014.

[10] M. A. Ismael and A. J. Chamkha, "Conjugate natural convection in a differentially heated composite enclosure filled with a nanofluid," *Journal of Porous Media*, vol. 18, no. 7, pp. 699–716, 2015.

[11] A. Tahmasebi, M. Mahdavi, and M. Ghalambaz, "Local thermal nonequilibrium conjugate natural convection heat transfer of nanofluids in a cavity partially filled with porous media using Buongiorno's model," *Numerical Heat Transfer, Part A: Applications*, vol. 73, no. 4, pp. 254–276, 2018.

[12] S. A. M. Mehryan, M. Ghalambaz, and M. Izadi, "Conjugate natural convection of nanofluids inside an enclosure filled by three layers of solid, porous medium and free nanofluid using Buongiorno's and local thermal non-equilibrium models," *Journal of Thermal Analysis and Calorimetry*, vol. 135, no. 2, pp. 1047–1067, 2019.

[13] A. I. Alsabery, A. J. Chamkha, H. Saleh, I. Hashim, and B. Chanane, "Darcian natural convection in an inclined trapezoidal cavity partly filled with a porous layer and partly with a nanofluid layer," *Sains Malaysiana*, vol. 46, no. 5, pp. 803–815, 2017.

[14] A. I. Alsabery, A. J. Chamkha, H. Saleh, and I. Hashim, "Natural convection flow of a nanofluid in an inclined square enclosure partially filled with a porous medium," *Scientific Reports*, vol. 7, no. 1, Article ID 2357, 2017.

[15] M. H. Toosi and M. Siavashi, "Two-phase mixture numerical simulation of natural convection of nanofluid flow in a cavity partially filled with porous media to enhance heat transfer," *Journal of Molecular Liquids*, vol. 238, pp. 553–569, 2017.

[16] A. M. J. Al-Zamily, "Analysis of natural convection and entropy generation in a cavity filled with multi-layers of porous medium and nanofluid with a heat generation," *International Journal of Heat and Mass Transfer*, vol. 106, pp. 1218–1231, 2017.

[17] M. T. Nguyen, A. M. Aly, and S.-W. Lee, "Effect of a wavy interface on the natural convection of a nanofluid in a cavity with a partially layered porous medium using the ISPH method," *Numerical Heat Transfer, Part A: Applications*, vol. 72, no. 1, pp. 68–88, 2017.

[18] A. I. Alsabery, M. A. Ismael, A. J. Chamkha, and I. Hashim, "Impact of finite wavy wall thickness on entropy generation and natural convection of nanofluid in cavity partially filled with non-Darcy porous layer," *Neural Computing and Applications*, vol. 32, no. 17, pp. 13679–13699, 2020.

[19] H. T. Kadhim, F. A. Jabbar, and A. Rona, "Cu–Al_2O_3 hybrid nanofluid natural convection in an inclined enclosure with wavy walls partially layered by porous medium," *International Journal of Mechanical Sciences*, vol. 186, Article ID 105889, 2020.

[20] I. V. Miroshnichenko, M. A. Sheremet, H. F. Oztop, and N. Abu-Hamdeh, "Natural convection of alumina–water nanofluid in an open cavity having multiple porous layers," *International Journal of Heat and Mass Transfer*, vol. 125, pp. 648–657, 2018.

[21] B. M. Al-Srayyih, S. Gao, and S. H. Hussain, "Natural convection flow of a hybrid nanofluid in a square enclosure partially filled with a porous medium using a thermal non-equilibrium model," *Physics of Fluids*, vol. 31, no. 4, Article ID 043609, 2019.

[22] A. J. Chamkha, S. Sazegar, E. Jamesahar, and M. Ghalambaz, "Thermal non-equilibrium heat transfer modeling of hybrid nanofluids in a structure composed of the layers of solid and porous media and free nanofluids," *Energies*, vol. 12, no. 3, Article ID 541, 2019.

[23] Z. A. S. Raizah, S. E. Ahmed, and A. M. Aly, "ISPH simulations of natural convection flow in E-enclosure filled with a nanofluid including homogeneous/heterogeneous porous media and solid particles," *International Journal of Heat and Mass Transfer*, vol. 160, Article ID 120153, 2020.

[24] F. Selimefendigil and A. J. Chamkha, "MHD mixed convection of Ag–MgO/water nanofluid in a triangular shape partitioned lid-driven square cavity involving a porous compound," *Journal of Thermal Analysis and Calorimetry*, vol. 143, no. 2, pp. 1467–1484, 2021.

[25] M. Ghalambaz, K. A. Ayoubloo, and A. Hajjar, "Melting heat transfer of a non-Newtonian phase change material in a cylindrical vertical-cavity partially filled porous media," *International Journal of Numerical Methods for Heat & Fluid Flow*, vol. 30, no. 7, pp. 3765–3789, 2019.

[26] M. Ghalambaz, S. A. M. Mehryan, K. A. Ayoubloo et al., "Thermal behavior and energy storage of a suspension of nano-encapsulated phase change materials in an enclosure," *Advanced Powder Technology*, vol. 32, no. 6, pp. 2004–2019, 2021.

[27] A. M. Aly and N. Alsedais, "Natural convection of NEPCM in a partial porous H-shaped cavity: ISPH simulation," *International Journal of Numerical Methods for Heat & Fluid Flow*, vol. 33, no. 6, pp. 2232–2249, 2023.

[28] A. Elliott, M. Torabi, N. Karimi, and S. Cunningham, "On the effects of internal heat sources upon forced convection in porous channels with asymmetric thick walls," *International Communications in Heat and Mass Transfer*, vol. 73, pp. 100–110, 2016.

[29] A. F. Baytaş and A. C. Baytaş, "Thermal non-equilibrium natural convection in a square enclosure with heat-generating porous layer on inner walls," *Transport in Porous Media*, vol. 120, no. 1, pp. 167–182, 2017.